(SWCNT) solids by using a spark plasma sintering and hot-pressing method, and investigated their mechanical properties and microstructures. Transmission electron microscope (TEM) and Raman analyses of the SWCNT solids revealed that the high-temperature treatment has transformed some parts of the SWCNTs into a graphite-like structure. Furthermore, structure changes of the SWCNTs were accelerated by increasing processing temperature (1000~1800 °C) under a pressure of 120 MPa in vacuum. In this study, to explore tribological properties and how the SWCNTs might react to the friction surface of the SWCNT solids, we employed three kinds of the SWCNT solids having different SWCNTs content. In order to compare the tribological properties of the SWCNT solids with those of other forms of carbon, the experiments were also performed with the bulk graphite material.

2. EXPERIMENTAL DETAILS

The binder-free macroscopic SWCNT solids were prepared by hot-pressing highly pure SWCNTs. The details of the experimental procedures and conditions of the SWCNT solids preparation were described elsewhere.[13, 15] The SWCNT solids were prepared by sintering the purified SWCNTs at temperatures of 1000 °C, 1400 °C, and 1800 °C under a pressure of 120 MPa in vacuum for 5 min in a 20.0-mm-diameter graphite die. The disk-shaped specimen, measuring 20.0-mm-diameter and 1.5-mm-thickness, was manufactured into $2 \times 1 \times 18$ mm for the measurement of the friction coefficient, and 3.5-mm-diameter and 1.0-mm-thickness for the measurement of specific wear rate, respectively. The plate and disk test pieces were sectioned from hot-pressed specimens such that the friction surface was perpendicular to the hot-pressing direction.

Figure 1 shows schematic illustrations of the two experimental set-ups which were used in the present work to evaluate the tribological properties of the SWCNT solids. The experiments with reciprocating ball-on-plate (experiment A in Table I) and pin-on-disk (experiment B in Table I) tribometer were conducted at a room temperature of 23 ± 2 °C and at a relative humidity of $40 \pm 10\%$. The commercially supplied 7.1-mm-diameter Si_3N_4 ball (Nihon Ceratec, Japan) and 30.0-mm-diameter and 4.0-mm-thickness Si_3N_4 disk (Japan Fine Ceramics, Japan) were used as counterparts. The friction coefficient (μ) was calculated by taking into account the normal load applied and the friction force measured using a strain gauge bridge. The specific wear rate (w_s) is defined as $w_s = \Delta V/(P \cdot L)$, ΔV is the mass loss, P is the normal load (2.0 N) and L is the sliding distance (1.0×10^5 m). Before the test, samples and counterparts were ultrasonically cleaned in ethanol for 15 min and then dried in an oven at 60 °C.

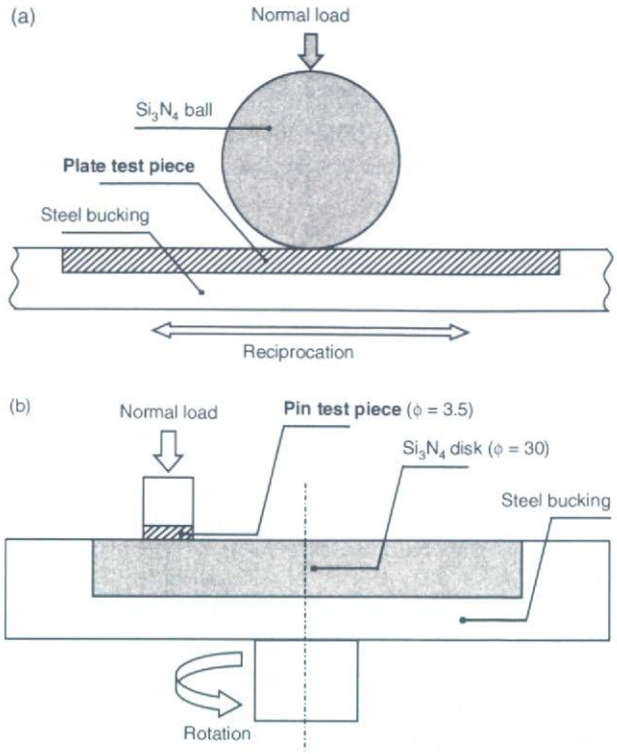

Fig. 1. Schematic diagram of test configurations: (a) reciprocating ball-on-plate tribometer and (b) pin-on-disk tribometer.

The surface roughness was measured on a laser noncontact 3D measuring machine (Mitaka Kohki NH-3T, Japan). Scanning electron microscopy (SEM; Hitachi S-4700, Japan) was used to investigate the microstructure. Raman spectroscopy (HORIBA T64000, Japan) with an Ar ion laser, was used to analyze the physical properties of the SWCNTs. Samples were measured by using a 488.0 nm exciting laser under the backscattering configuration at room temperature.

Table I. The densities, mechanical properties and initial surface roughness of the SWCNT solids and bulk graphite material.

Experiment	Velocity (cm/s)	Load (N)	Test materials	Density ρ, (Mg/m^3)	Young's modulus E_b, (GPa)	Flexural strength O_b, (MPa)	Surface roughness R_a, (μm)
A	2.0	2.0	SWCNT solid (1000 °C)	1.39	2.0	11.6	0.14
			SWCNT solid (1400 °C)	1.54	7.5	34.8	0.10
			SWCNT solid (1800 °C)	1.70	19.6	89.3	0.08
			Bulk graphite material	1.58	5.9	36.1	0.11
B	20.0	2.0	SWCNT solid (1000 °C)	1.39	2.0	11.6	0.14
			Bulk graphite material	1.58	5.9	36.1	0.07

3. RESULTS AND DISCUSSION

The densities, mechanical properties and initial surface roughness (R_a) of the SWCNT solids and bulk graphite material are listed in Table I. Some earlier data and experimental details for the mechanical evaluation of the SWCNT solids are given in.[13] It is seen in Table I that the mechanical properties of the SWCNT solids are strongly dependent on the processing temperature. The reason for the increase in the mechanical properties such as Young's modulus and flexural strength may be due to the effective suppression of slide deformation between SWCNT bundles,[13, 15] through the formation of stable links between SWCNTs, although their values are significantly lower than those of individual SWCNTs. The R_a of the SWCNT solids ranged from 0.08 to 0.18 μm, and they seemed to decrease with increasing processing temperature. The R_a of the Si_3N_4 ball and disk were 0.05 and 0.13 μm, respectively.

The typical variation of friction coefficients with respect to the sliding distance of the SWCNT solids and bulk graphite material is shown in Figure 2. After an initial break-in period of about a 0.5 m sliding distance, friction coefficients for all the SWCNT solids started to get somewhat steady and remain very stable until the end of test, indicating that the SWCNTs were immediately efficient in the transient period. The steady-state friction coefficients, calculated by averaging the values for the last 50% of the sliding distance, were 0.23, 0.22, 0.24 and 0.20 for the SWCNT solids prepared at 1000 °C, 1400 °C 1800 °C and bulk graphite material, respectively. There was no clear difference in friction coefficients among all the SWCNT solids. However, friction coefficient of the SWCNT solids seemed to be slightly higher than that of bulk graphite material.

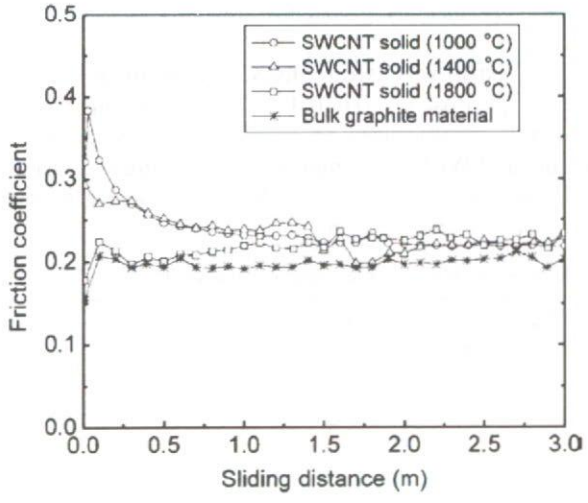

Fig. 2. Friction behavior of the SWCNT solids prepared at 1000 °C, 1400 °C, 1800 °C and bulk graphite material.

To understand the friction behavior, microscopic examinations were carried out on the friction surface. Figures 3 and 4 show the SEM images and cross-sectional surface profiles of the friction surface on the SWCNT solid prepared at (a) 1000 °C, (b) 1400 °C, (c) 1800 °C and (d) bulk graphite material, respectively. For the SWCNT solid prepared at 1000 °C, a considerably roughened surface and plastic deformation with a characteristic groove parallel to the sliding direction were observed as shown in Figures 3(a) and 4(a). These phenomena seemed to correlate with the poor elasticity against Si_3N_4 counterpart. When the processing temperature is higher, (Figs. 3(b) and 4(b)), on the other hand, the plastic deformation on the friction surface was greatly reduced due to its higher elasticity. Moreover, there was no clear difference between friction surface of the SWCNT solids prepared at 1800 °C (Figs. 3(c) and 4(c)) and bulk graphite material (Figs. 3(d) and 4(d)). Figure 5 shows a high-magnification SEM image of the friction surface on the SWCNT solids prepared at 1000 °C, in which several cracks perpendicular to the sliding direction were observed. Some of the SWCNTs were still present in the cracks, although no SWCNT structure was observed on the friction surface. Thus, the SWCNTs that existed in the friction surface may have been damaged and deformed during sliding, which resulted in a film-like structure, namely transferred film.

We now summarize another set of experiments (experiment B in Table I). The SWCNT solid prepared at 1000 °C is used to determine the structure changes of the SWCNTs induced by friction surface. In the present experiment, the SWCNT solid was used as flat-ended pin in the tribometer (Fig. 1(b)). The steady-state friction coefficient and specific wear rate of the SWCNT solid were 0.23 and 1.3×10^{-4} mm^3/Nm, respectively. The friction coefficient obtained from the present experiment showed a value similar to that obtained by the experiment using the ball-on-plate tribometer. On the other hand, specific wear rate of the SWCNT solid was about two orders of magnitude inferior to that of bulk graphite material (9.0×10^{-6} mm^3/Nm).

Post-test microscopic and physical analyses of the virgin and friction surface of the SWCNT solid, thin film-like substance on the counterpart and wear debris provided information that helped to elucidate the friction and wear mechanisms. Figure 6 shows the SEM images of the friction surface on the SWCNT solid and thin film-like substance on the counterpart. As seen in Figure 6(a), a roughened surface with well defined grooves parallel to the sliding direction was observed. The enlarged SEM image shows regularly pushed down SWCNTs, which resemble a compressed spaghetti structure. However, most of the friction surface seemed to be covered with the above-mentioned transferred film, as shown at the right-side of the enlarged SEM image. Figure 6(b) shows the SEM image of the thin film-like substance on the counterpart. Friction surface on the counterpart seemed to be covered with the transferred film just like friction surface on

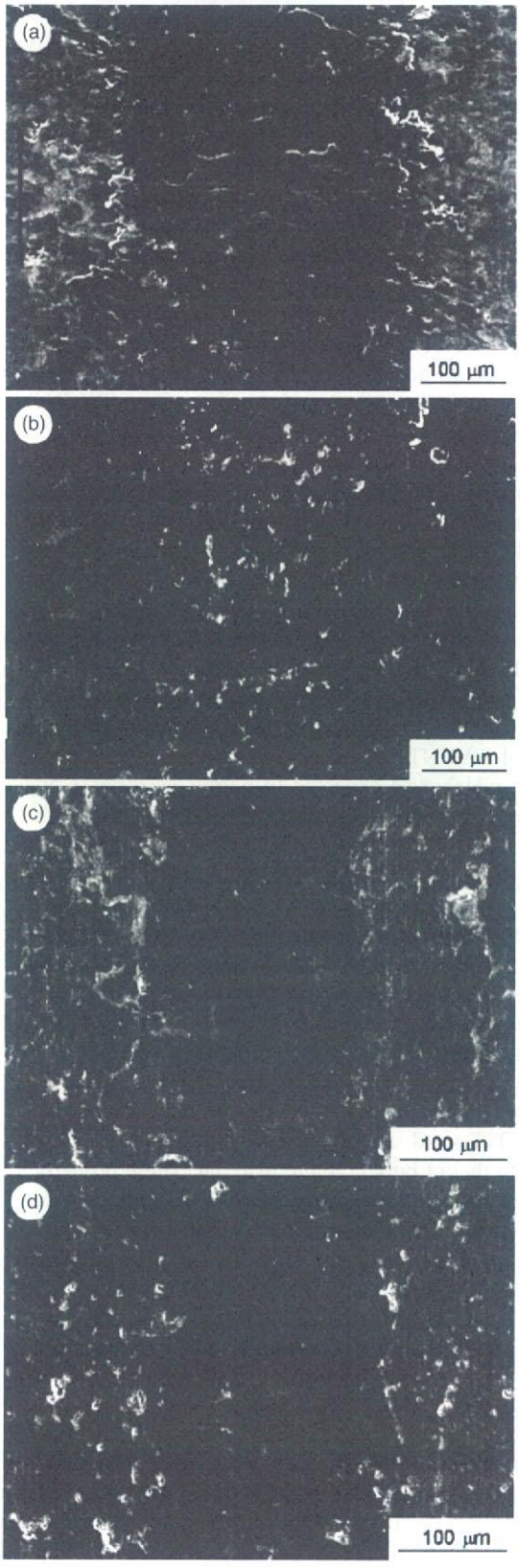

Fig. 3. SEM images of the friction surface on the SWCNT solids prepared at (a) 1000 °C, (b) 1400 °C, (c) 1800 °C and (d) bulk graphite material, respectively. The arrow indicates the sliding direction.

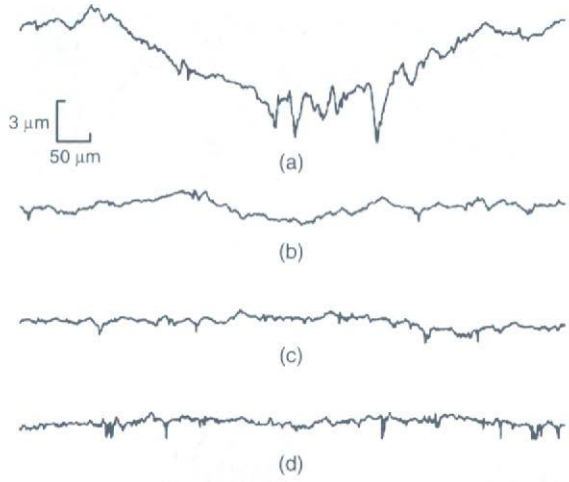

Fig. 4. Cross-sectional surface profiles of the friction surface on the SWCNT solids prepared at (a) 1000 °C, (b) 1400 °C, (c) 1800 °C and (d) bulk graphite material, respectively.

the SWCNT solid, in which we can hardly observe the SWCNT structure.

To obtain an in-depth understanding of the surface structure changes, Raman spectra were obtained for the virgin and friction surface of the SWCNT solid, thin film-like substance on the counterpart and wear debris. Figure 7 shows the typical Raman spectrum of the above-mentioned four samples that have been subjected to tribological evaluation using the pin-on-disk tribometer. The processing temperature for the sample tested was 1000 °C. Raman intensity ratios between peaks at 1590 cm^{-1} and 1350 cm^{-1} (I_G/I_D) are also indicated in Figure 7. Raman-scattering peaks corresponding to E_{2g} vibration mode near 1568 and 1590 cm^{-1} are due to the zone-folding effect of the SWCNTs. Since the peak at 1350 cm^{-1} corresponds to a Raman-active mode of defective carbon network, the intensity is roughly proportional to the amount of amorphous carbon in the sample.[16, 17] The relative

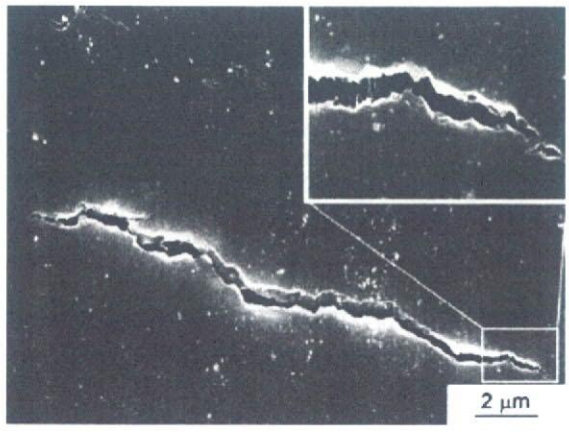

Fig. 5. High-magnification SEM image of the friction surface on the SWCNT solids prepared at 1000 °C. The arrow indicates the sliding direction.

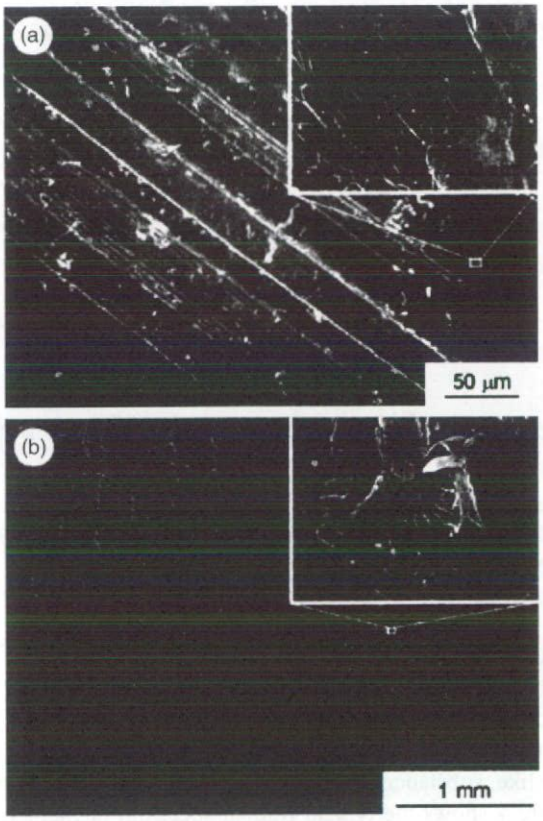

Fig. 6. SEM images of the friction surface on (a) SWCNT solid prepared at 1000 °C and (b) Si_3N_4 counterpart, respectively. The arrow indicates the sliding direction.

Raman-scattering intensity ratio I_G/I_D of the peaks at 1350 cm^{-1} (D-band) and 1590 cm^{-1} (G-band) is a convenient measure of the purity of SWCNTs in the sample.[18, 19] In Figure 7(a) the characteristic multiply split peaks at

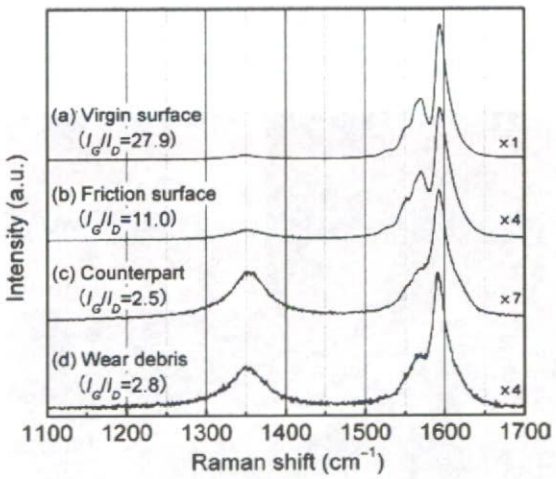

Fig. 7. Raman spectra of (a) virgin and (b) friction surface of the SWCNT solid prepared at 1000 °C, (c) thin film-like substance on the counterpart and (d) wear debris, respectively. The Raman-scattering intensity ratio I_G/I_D estimated from the peak position of the D-band and G-band are also indicated.

1569 and 1593 cm^{-1}, and the shoulder at 1550 cm^{-1} were clearly observed in the virgin surface on the SWCNT solid, providing definitive evidence for the presence of SWCNTs. In the friction surface on the SWCNT solid, a broad peak at 1350 cm^{-1} appeared at the same time, I_G/I_D decreased from 27.9 to 11.0, indicating a formation of some amorphous carbon during sliding. The higher and broader peak at 1350 cm^{-1} was observed in the spectrum of the thin film-like substance on the counterpart and wear debris. Furthermore, apparent multiply split peaks disappeared. This may be attributed to the structure changes of SWCNTs, as they lost their tube-structural features and hence could not produce the multiply splits. These results may also support the transformation of the SWCNTs during sliding.

According to the SEM and Raman data, in conjunction with the friction behavior of the SWCNT solids and bulk graphite material, the following friction mechanism may be deduced. The microstructural observations showed that the transferred film containing SWCNTs existed on the friction surface (Figs. 6(a) and (b)), suggesting that the sliding between SWCNTs composed of amorphous carbon occurred at the interface of the sliding couples, which was also confirmed by additional Raman analysis (Fig. 7). The resultant friction behaviors may be related to the smearing of SWCNT-derived amorphous carbon over the contact area, which was expected to permit easy shear and then help to achieve a lubricating effect during sliding.

4. CONCLUSIONS

In this study, tribological properties and SWCNTs reactions to the friction surface of the SWCNT solids were investigated. The friction coefficients of the SWCNT solids were found to reach values as low as 0.22–0.24, according to unidirectional sliding friction tests using Si_3N_4 counterpart in air, which values were slightly higher than that of bulk graphite material. The specific wear rate of the SWCNT solid was about two orders of magnitude inferior to that of bulk graphite material. These properties may be related to the formation of SWCNT-derived transferred film made up of amorphous carbon between the sliding couples. The mechanism of formation of transferred film is for the moment ambiguous. The most probable hypothesis based on the SEM and Raman data is that SWCNT may have transformed into a more stable structure during sliding, which may be a possible reason for the low friction coefficient of the SWCNT solids.

Acknowledgments: This work was supported by the 21st Century Center of Excellence (COE) Program Grant of the International COE of Flow Dynamics, Ministry of Education, Culture, Sports, Science and Technology. The authors thank Prof. K. Tohji and Dr. Y. Sato of Graduate School of Environmental Studies, Tohoku University for useful information and discussion. G. Y.

thanks Dr. B. Stoimenov of Bio-Mimetic Control Research Center, RIKEN and, Dr. H. Miki and Mr. N. Yoshida of Institute of Fluid Science, Tohoku University for their technical support.

References and Notes

1. K. Miyoshi, Solid Lubrication Fundamental and Applications, Marcel Dekker, Inc., New York (**2001**).
2. S. Kitaoka, T. Tsuji, T. Katoh, Y. Yamaguchi, and K. Kashiwagi, *J. Am. Ceram. Soc.* 77, 1851 (**1994**).
3. M. Chen, K. Kato, and K. Adachi, *Wear* 250, 246 (**2001**).
4. H. W. Kroto, J. R. Heath, S. C. O'Brien, R. F. Curl, and R. E. Smalley, *Nature* 318, 162 (**1985**).
5. U. D. Schwarz, O. Zworner, P. Koster, and R. Wiesendanger, *Phys. Rev. B* 56, 6987 (**1997**).
6. S. W. Lee, Y. S. Shon, T. R. Lee, and S. S. Perry, *Thin Solid Films* 358, 152 (**2000**).
7. A. Tanaka, K. Umeda, M. Yudasaka, M. Suzuki, T. Ohana, M. Yumura, and S. Iijima, *Tribol. Lett.* 19, 135 (**2005**).
8. J. W. An, D. H. You, and D. S. Lim, *Wear* 255, 677 (**2003**).
9. D. S. Lim, D. H. You, H. J. Choi, S. H. Lim, and H. Jang, *Wear* 259, 539 (**2005**).
10. J. P. Tu, Y. Z. Yang, L. Y. Wang, X. C. Ma, and X. B. Zhang, *Tribol. Lett.* 10, 225 (**2001**).
11. W. X. Chen, J. P. Tu, L. Y. Wang, H. Y. Gan, Z. D. Xu, and X. B. Zhang, *Carbon* 41, 215 (**2003**).
12. B. Dong, Z. Yang, Y. Huang, and H. L. Li, *Tribol. Lett.* 20, 251 (**2005**).
13. G. Yamamoto, M. Omori, Y. Sato, T. Takahashi, K. Tohji, and T. Hashida, *JSME Int. J. Ser. A-Solid Mech. Mat. Eng.* 48, 189 (**2005**).
14. G. Yamamoto, Y. Sato, T. Takahashi, M. Omori, A. Okubo, K. Tohji, and T. Hashida, *Scr. Mater.* 54, 299 (**2005**).
15. G. Yamamoto, Y. Sato, T. Takahashi, M. Omori, T. Hashida, A. Okubo, and K. Tohji, *J. Mater. Res.* 21, 1537 (**2006**).
16. R. Saito, G. Dresselhaus, and M. S. Dresselhaus, Physical Properties of Carbon Nanotubes, Imperial College Press, London (**1998**).
17. M. S. Dresselhaus, G. Dresselhaus, A. Jorio, A. G. Souza Filho, and R. Saito, *Carbon* 40, 2043 (**2002**).
18. H. Kataura, Y. Kumazawa, Y. Maniwa, Y. Ohtsuka, R. Sen, S. Suzuki, and Y. Achiba, *Carbon* 38, 1691 (**2000**).
19. Y. Sato, B. Jeyadevan, R. Hatakeyama, A. Kasuya, and K. Tohji, *Chem. Phys. Lett.* 385, 323 (**2004**).

Received: 11 December 2006. Accepted: 10 April 2007.

Journal of Solid Mechanics and Materials Engineering

Vol. 1, No. 7, 2007

Mechanical Properties of Single-Walled Carbon Nanotube Solids Prepared by Spark Plasma Sintering*

Go YAMAMOTO**, ***, Yoshinori SATO***, Toru TAKAHASHI****, Mamoru OMORI****, Kazuyuki TOHJI*** and Toshiyuki HASHIDA****

**Institute of Fluid Science, Tohoku University,
2-2-1 Kataura, Aoba-ku, Sendai 980-8577, Japan
E-mail: gyamamoto@rift.mech.tohoku.ac.jp
***Graduate School of Environmental Studies, Tohoku University,
6-6-11-1305, Aza-Aoba, Aramaki, Aobaku, Sendai 980-8579, Japan
****Fracture and Reliability Research Institute, Tohoku University,
6-6-11-707, Aza-Aoba, Aramaki, Aobaku, Sendai 980-8579, Japan

Abstract

In this paper, a spark plasma sintering (SPS) method was employed to solidify single-walled carbon nanotubes (SWCNTs) only, and the effect of processing conditions on the mechanical properties of the SWCNT solids were examined using a small punch (SP) testing method. The sintering temperatures used was in the range of 600~1400°C, and the sintering pressures used was 40 MPa and 120 MPa. It was demonstrated that the SPS method allowed SWCNTs to be solidified, without any additives. The experimental results showed that the purification of raw soot was critically importance. The SWCNT solids prepared from purified raw soot showed significant non-linear deformation response, producing quasi-ductile fracture behavior. In contrast, raw soot produced brittle solids. The Young's modulus, fracture strength and work of fracture increased with the increasing sintering temperature and pressure. The Raman and SEM analyses showed that the amount of the graphite-like materials were observed to increase with the increasing temperature and pressure, which indicate that the structure of the SWCNTs was changed partially into the graphite-like materials. The formation of graphite-like materials increased tendency of brittle fracture in the SWCNT solids. TEM observations revealed that the fracture surfaces of the SWCNT solids were characterized by pull out of SWCNT bundles. This observation suggests that it may be possible to improve the mechanical properties of SWCNT solids by increasing the cohesion between SWCNTs.

Key words: Single-Walled Carbon Nanotube, Spark Plasma Sintering Method, Small Punch Testing Method, Young's Modulus, Work of Fracture

1. Introduction

Recent experimental studies have amply demonstrated that individual single-walled carbon nanotubes [1][2] (SWCNTs) have an extremely high Young's modulus and tensile strength [3]-[5]. Researchers have mostly examined the possible applications of SWCNTs in various matrices, and characterized the properties and microstructures of these composite materials [6][7]. However, the production of SWCNT-reinforced composites with unprecedented mechanical properties is yet to be realized. Additionally, in order to take full

*Received 25 Dec., 2006 (No. T-04-0645)
Japanese Original : Trans. Jpn. Soc. Mech. Eng., Vol. 71, No. 702, A (2005), pp.330-337 (Received 3 June, 2004)
[DOI: 10.1299/jmmp.1.854]

advantage of the intrinsic mechanical and physical properties of SWCNTs, it is necessary to produce solid structures that are composed solely of the SWCNTs.

In this study, we have successfully produced binder-free SWCNT solids with purified SWCNTs by using a spark plasma sintering (SPS) method [8], and the mechanical properties of the disk specimens were investigated by a small punch (SP) testing method [9]. Here, the effects of processing temperatures and pressures on the mechanical properties of the resultant solids were investigated. Raw soot synthesized by conventional methods commonly contains metal particles and various forms of carbon. Therefore, the effect of the impurities on the mechanical properties and microstructures was also investigated by comparing the results obtained from the disk specimens made of the purified SWCNTs and raw soot containing by-products and SWCNTs.

2. Experimental

2.1 Purification Procedure for SWCNTs and Solidification Method

SWCNTs were synthesized by a direct current arc discharge between a pure graphite cathode and a metal loaded graphite anode [10]. A pure graphite rod (Wako Pure Chemical Industries, 99.9 % purity), 16 mm in diameter and 50 mm in length, and a 6 mm in diameter and 80 mm in length graphite rod loaded with Fe and Ni powders (Wako Pure Chemical Industries, 99.99 % purity) were used as cathode and anode, respectively. The mixing ratio of Fe, Ni and graphite powder for synthesis of SWCNTs was 1:1:3 by weight. The arc discharge was carried out under a helium atmosphere of 100 Torr. The discharge current was 70 A, and during the discharge, the gap between the electrodes was maintained at about 3 mm by manually advancing the consumed anode. The raw soot containing SWCNTs produced by the arc discharge method was retrieved from the upper wall and the roof of the chamber and was homogenized by mixing together regardless of the different sampling locations. In the raw soot, SWCNTs coexist with many by-products such as metal particles, fullerenes and amorphous carbon. Therefore, SWCNTs were separated step by step from the impurities using the following purification process. First, the fullerenes and the amorphous carbon were burned out by heating approximately 600 mg of raw soot at 450°C and keeping for 30 min in air. Then, the residual soot was heated up to 500°C and kept for 30 min in air to burn out the graphitic layers surrounding metal particles. Finally, the metal particles were washed out from the soot by treating with 6 M hydrochloric acid solution. The processed soot was filtered and rinsed with deionized water.

Purified SWCNTs and raw soot were solidified by using the SPS technique in a graphite die with an inner diameter of 10 mm. The processing temperatures and pressures used for preparation of disk specimens are summarized in Table 1. After applying the given pressure, the samples were heated to the desired temperature and held at this temperature for 5 min. The prepared specimens were disk-shaped about 10 mm in diameter and 1.5~1.8 mm in thickness, and were then polished with emery paper (#4000) into 10 mm in diameter and 1.2 mm in thickness. Purified SWCNTs was also consolidated by mechanical compaction only at room temperature and pressures of 40 and 120 MPa.

Table 1 Processing conditions of SWCNT solids prepared by spark plasma sintering.

Materials	Sintering temperature (°C)	Sintering pressure (MPa)	Holding time (min)
Raw soot	1000	120	5
Purified SWCNTs	600-1400	40, 120	5

2.2 Evaluation Method

The mechanical properties such as Young's modulus and work of fracture were measured by the SPS testing method using miniaturized disk specimens. Figure 1 shows schematic illustration of the experimental setup which was used in the present work to evaluate the mechanical properties of the SWCNT solids. The SP tests were performed on a universal testing machine (Instron 1185, Instron Corporation) in atmospheric conditions at room temperature. The disk specimens were placed on a die having a central borehole and simply supported on the circular edge. The load was applied at the specimen center through a puncher at a crosshead speed of 0.05 mm/min. The displacement of the specimens was monitored at the mid-point using a linear variable differential transducer (LVDT; DTH-A-50, Kyowa Electronic Instruments) fixed on to the testing machine.

Deformation and stress analysis for SP tests have been performed using an element method (FEM), assuming liner elastic response of the material [9]. In this study, the numerical data were used to compute Young's modulus and to construct stress-normalized displacement diagram. The Young's modulus of SP specimen E_{SP} was calculated from the measured initial linear slope of the load-displacement curve, which was expressed by the following equation:

$$E_{SP} = f(t/a)\frac{3a^2P(1-\nu)(3+\nu)}{4\delta\pi t^3} = f(t/a)\frac{P}{\delta}C_0, \tag{1}$$

where P is the load, δ the displacement measured at the specimen center, $f(t/a)$ the correction factor for the specimen thickness, a the borehole diameter of the supporting die (=2.1 mm), ν the Poisson's ratio, and t the specimen thickness (=1.2 mm). The maximum tensile stress along the load application point σ_{SP} can be expressed by the equation given below.

$$\sigma_{SP} = \frac{P}{t^2}(1+\nu)\left[0.485\ln\frac{a}{t} + 0.52 + \frac{3}{2\pi(1+\nu)}\right] = \frac{S_0}{t^2}P. \tag{2}$$

Equations (1) and (2) suggest that plotting the stress versus normalized displacement curve (σ_{SP}-$[S_0/f(t/a)C_0t]\delta$) provides an initial slope of Young's modulus E_{SP}. The work of fracture was calculated using the area of the stress-normalized displacement curve up to the maximum load. The disk specimens made of purified SWCNTs and raw soot are referred to

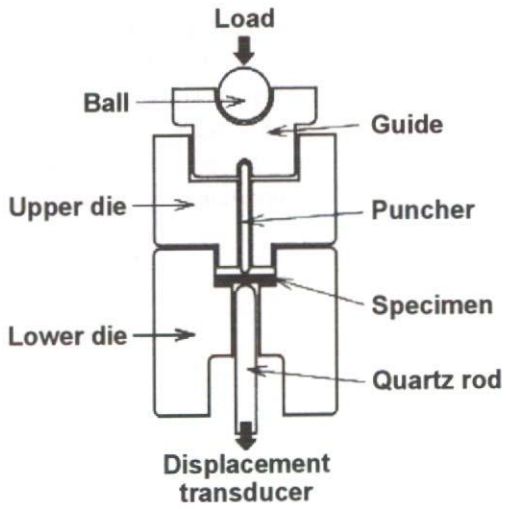

Fig. 1 Schematic illustration of small punch testing method.

as SWCNT solid and raw soot solid, respectively. For each processing condition, two specimens were tested and the averaged results will be presented below.

The structural analysis of the purified SWCNTs and raw soot was carried out using a Raman spectroscopy (T64000, HORIBA) with Ar ion laser, powder X-ray diffractometer (M21, Mac Science) with Cu Kα X-ray source and scanning electron microscopy (SEM; S-4700, Hitachi). The fracture surface was investigated by using a transmission electron microscopy (TEM; HF-2000, Hitachi).

3. Results and Discussion

3.1 Evaluation of the Purification Procedure and Characterization of Purified SWCNTs

In this study, macroscopic SWCNT solid was successfully solidified by SPS. Figures 2 and 3 show the Raman spectrum of the raw soot and purified SWCNTs, respectively. Abundance of SWCNTs in the each sample estimated from the Raman-scattering intensity ratio I_G/I_D is also indicated. Raman-scattering peaks corresponding to E_{2g} vibration mode near 1570 and 1590 cm^{-1} are due to the zone-folding effect of the SWCNTs [11]. Since the peak at 1350 cm^{-1} corresponds to a Raman-active mode of defective carbon network, the intensity roughly proportional to the amount of amorphous carbon in the sample. Hence, the relative Raman-scattering intensity ratio I_G/I_D of the peaks at 1350 cm^{-1} (D-band) and 1590 cm^{-1} (G-band) is a convenient index for the evaluation of SWCNT abundance ratio in the sample. It can be seen from Figs. 2 and 3 that the G-band peak intensity of the purified SWCNTs increased from 14.5 to 96.4 compared with that of the raw soot. Furthermore, the I_G/I_D of the purified SWCNTs was about seven times larger than that of raw soot, without any change in each peak position. Figures 4 and 5 show the typical SEM images of the raw

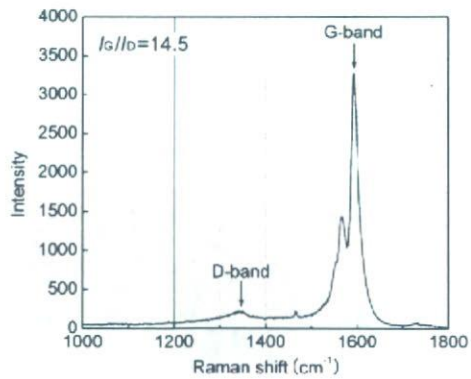

Fig. 2 Raman spectrum of the raw soot.

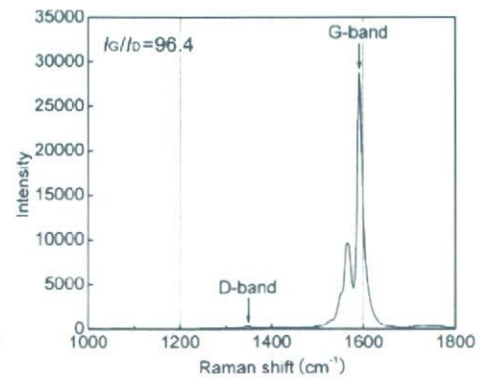

Fig. 3 Raman spectrum of the purified SWCNTs.

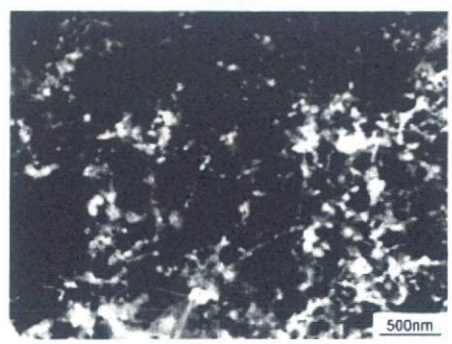

Fig. 4 SEM image of the raw soot.

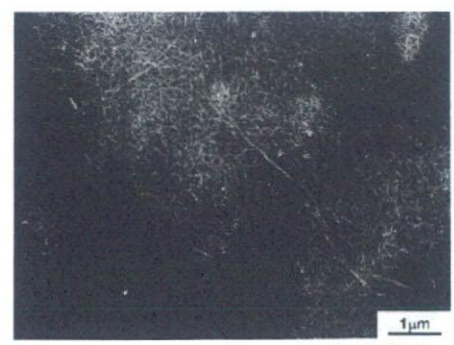

Fig. 5 SEM image of the purified SWCNTs.

soot and purified SWCNTs, respectively. The SEM image of the raw soot shows the SWCNT bundles coexisted with many by-products such as amorphous carbon. According to the XRD analysis of the raw soot [12], data shows the presence of C_{60}, graphite and metals. In contrast, the purified SWCNT were free of C_{60} and metals, showing only graphite peak. However, a trace amount of carbon materials with about 0.5 mm in diameter other than SWCNTs was observed as shown in Fig. 5. The length and diameter of the purified SWCNT bundle, estimated using SEM, were about 3~22 μm and 87 nm, respectively. These results suggest that highly pure SWCNTs have been obtained under the above-mentioned conditions, even though only a trace amount of carbon materials are present in the purified SWCNTs. The high purity of the SWCNT prepared has also been supported by thermogravimetric analysis.

3.2 Evaluation of Mechanical Properties

3.2.1 Effect of Impurities

In this work, we have successfully produced SWCNT solids with out any additives by using SPS method. Here, in order to reveal the effect of impurities on mechanical properties of the SWCNT solids, purified SWCNTs and raw soot were solidified by using the SPS method. The sintering temperature and pressure used for preparation of disk specimens are 1000°C and 120 MPa.

Figures 6 and 7 show the fractured specimens and stress-normalized displacement curves for both specimens, respectively. In the case of the raw soot solids, the main crack was formed at the center of the specimen that was subjected to the maximum biaxial stress and propagated to the outer region as shown in Fig. 6(a). The specimen was broken into four pieces, which demonstrated the brittle nature of the fracture. This observation corresponds to the deformation response as shown in Fig. 7. In contrast, the purified SWCNTs produced quasi-ductile solid structures. A fractured specimen is shown in Fig. 6(b), which is also illustrated schematically in Fig. 6(c). An indentation was formed on the specimen by the spherical puncher used for load application, and the main fracture initiated and propagated from a cone-shaped region at the edge of the indentation. A significant non-linear deformation response was observed for the SWCNT solids as shown in Fig. 7.

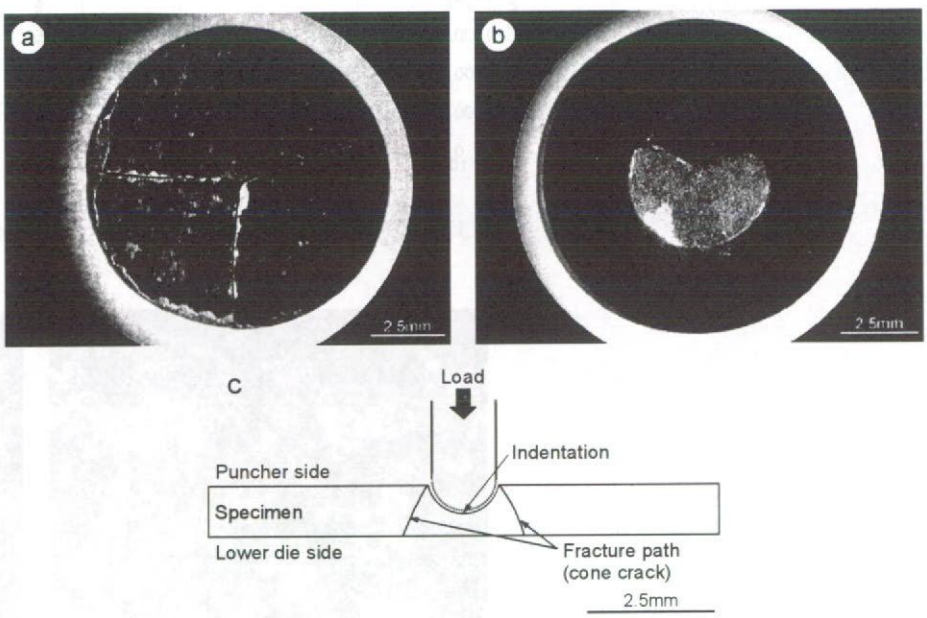

Fig. 6 Crack propagation of the (a) raw soot and (b) purified SWCNTs. Schematic illustration of the purified SWCNTs in also shown in (c).

The physical and mechanical properties for both specimens are shown in Table 2. The bulk density of the raw soot solids was found to be lager than that of the SWCNTs solids. This may be due to the presence of by-products such as metal particles, fullerenes and carbon materials in the raw soot solids. According to the density of raw soot solids, mass ratio of the metals contained in the raw soot is about 50 mass%. However, there was almost no difference in Young's modulus between the specimens. On the other hand, the work of fracture of the SWCNT solids was 12.4 times larger than that of the raw soot solids. The reason for the significant difference in the work of fracture may be due to the quasi-ductile fracture behavior of the SWCNT solids.

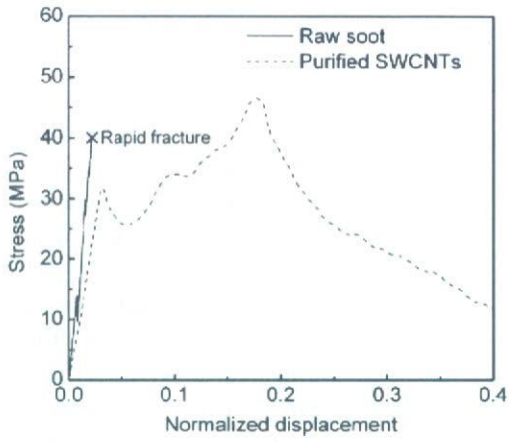

Fig. 7 Relation between stress and normalized displacement. (Processing condition: 1000°C, 120 MPa)

Table 2 Processing conditions and mechanical properties on the raw soot and purified SWCNTs prepared by spark plasma sintering.

Materials	Bulk density (Mg/m^3)	Young's modulus E_{SP} (GPa)	Work of fracture J_{SP} (N·mm)
Raw soot	1.90	0.76	1.4
Purified SWCNTs	1.55	0.66	17.3

3.2.2 Effects of Sintering Temperatures and Pressures

The effects of sintering temperatures and pressures on mechanical properties of the SWCNT solids were investigated. Here, the starting material used for preparation of solids is above-mentioned purified SWCNTs. Figure 8 shows the bulk density of the SWCNT solids as a function of sintering temperature. The theoretical density of individual SWCNTs has been calculated to be 1.36 Mg/m^3 [13][14], assuming the diameter of the SWCNTs to be 1.3 nm, and the distance between neighboring SWCNTs is determined by the van der Waals interaction. In the case of sintering pressure of 120 MPa, the density of the SWCNT solids tend to increase with the increasing sintering temperature and level off at about 1000°C. The saturation value is close to 1.6 Mg/m^3. On the other hand, the density of the SWCNT solids prepared at 40 MPa appears to at approximately 1200°C, and the saturation value is about 1.3 Mg/m^3. The reason for the density increase may be due to the structural change of the SWCNTs. It is well-known that the SPS technique is a pressure-assisted fast sintering method based on high-temperature plasma momentary generated in the gaps between powder materials by electrical discharge during on-off dc pulsing. It has been suggested that the dc pulse caused generate several effects such as spark plasma, spark impact, Joule

heating and an electrical diffusion [8]. Through these effects, it is expected that the density of the SWCNT solids give higher value than the theoretical density of individual SWCNTs.

The experimental measurements revealed that the mechanical properties of the SWCNT solids were dependent on the sintering temperature and pressure. Figure 9 gives typical load-displacement curves of the SWCNT solids determined from SP tests. Here, the sintering pressure used for preparation of SWCNT solids is 120 MPa. In all the specimens, cone-shaped fracture behavior was observed as shown in Figs. 6 (b) and (c). The nonlinear deformation response is observed up to the peak load followed by a long tail, for all the specimens. It is also seen that the initial slope and the peak load of the SWCNT solids increase with the increasing temperature. No clear change of the displacement at the maximum load was observed up to 1200°C, except for the SWCNT solids prepared at 1400°C. This phenomenon seems to correlate with the brittleness of the SWCNT solids prepared at 1400°C.

The Young's modulus E_{SP} of the SWCNT solids is plotted as a function of the sintering temperature in Fig. 10. It can be seen that the Young's modulus of the SWCNT solids increases with the increasing sintering temperature, in which the SWCNT solids prepared at 120 MPa gives higher value than that of SWCNT solids prepared at 40 MPa. However, it is unclear why the reduction in the Young's modulus occurs in the SWCNT solids prepared at a temperature of 1400°C and a pressure of 40 MPa.

Figure 11 shows the work of fracture of the SWCNT solids as a function of the processing temperature. It is seen that the variation of work of fracture with the processing conditions is approximately similar to that of the Young's modulus, except for the SWCNT solids prepared at a temperature of 1400°C and a pressure of 120 MPa. The reason for the drastic decrease may be due to the brittle fracture behavior as shown in Fig. 9.

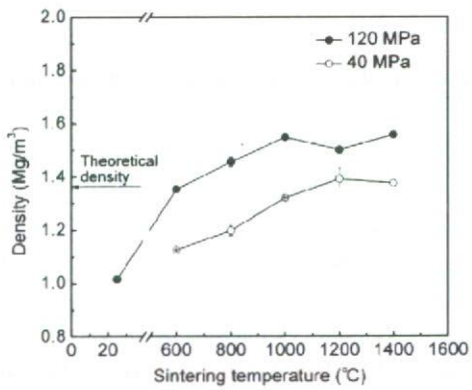

Fig. 8 Bulk densities of the SWCNT solids.

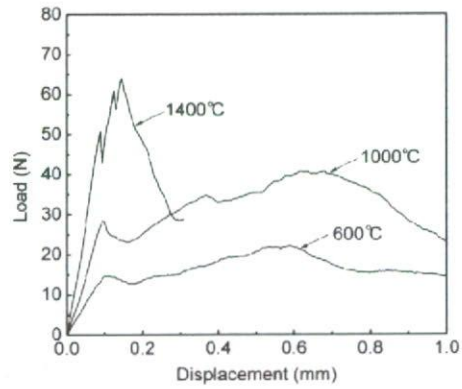

Fig. 9 Fracture behavior of the of the SWCNT solids.

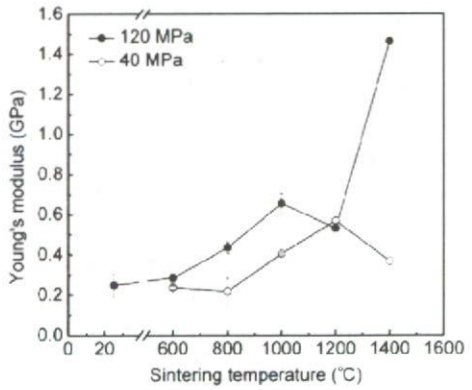

Fig. 10 Work of fracture of the SWCNT solids.

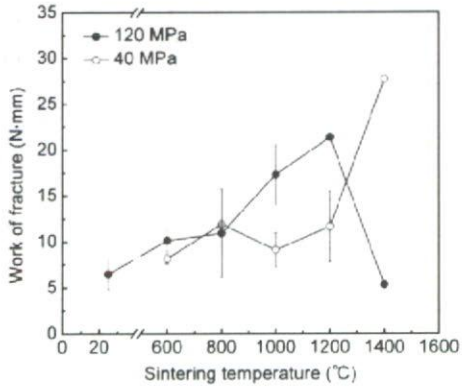

Fig. 11 Young's modulus of the SWCNT solids.

3.3 Microstructural Observation of the SWCNT Solid

The effects of sintering temperatures and pressures on nanostructure of the SWCNT solids were investigated. Figure 12 shows the Raman intensity ratio (I_G/I_D) for the SWCNT solids prepared under various processing conditions. Here, the I_G/I_D was normalized using the result of the SWCNT solids (I_G/I_D =70.0) consolidated by mechanical compaction only at room temperature and a pressure of 120 MPa. As shown in Fig. 12, the I_G/I_D of the SWCNT solids consolidated by mechanical compaction at room temperature was independent of the applied pressure. However, the I_G/I_D gradually decreased with increasing temperature and pressure, suggesting the transformation of SWCNTs into more stable structure. However, the Raman analysis provides no information about the structure of the SWCNT solids. Thus, we also carried out the microstructural observations of the SWCNT solids prepared under the various conditions.

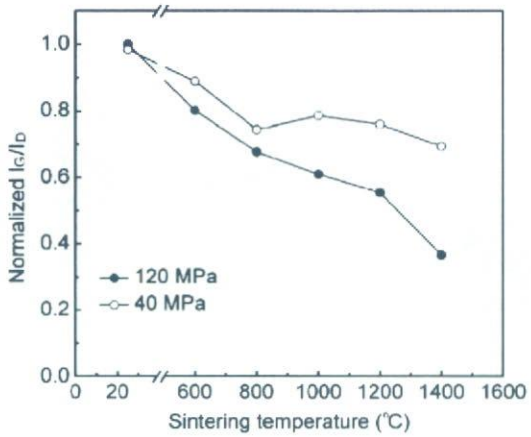

Fig. 12 Normalized IG/ID of the SWCNT solids as a function of sintering temperature.

Microstructural observations were carried out using SEM and TEM. Figure 13 shows a typical SEM image of fracture surface for the SWCNT solids prepared at a temperature of 1200°C and a pressure of 120 MPa. Extensive "pullout" of SWCNT bundles with approximately 3 μm in length was observed and the diameter of bundles was observed to decrease toward their tips. These experimental results indicate that the failure in the SWCNT solids prepared at lower sintering temperature occurred via sliding along the bundle surface or intra-bundles sliding between SWCNTs. The nonlinear deformation response of the SWCNT solids may be due to the pullout behavior of the bundles associated with the slippage of SWCNTs held by weak van der Waals interaction. Figures 14 and 15 show the typical TEM images of structure and fracture surface of the SWCNT solid prepared at a temperature of 600°C and a pressure of 120 MPa. It is seen that the bulk body provides a laminated structure of SWCNT bundles. As shown in Fig. 15, TEM image shows the SWCNT bundles contain 10~30 nanotubes extruding from the fracture surface. Detailed observation of the pullout bundles indicates that no breakage of SWCNTs occurred in the bundles. However, when the processing temperature was increased, the pulled out region was observed to decrease. As seen in Fig. 16, only a limited extent of pullout is observed in the SWCNT solid prepared at 1400°C. The pullout length of the bundles was obviously shorter, and the number of SWCNT bundles present was less than that of the SWCNT solids prepared at 600°C. It is noted that the outer surface of the bundles in the SWCNT solids prepared at 1400°C is much rougher than that of the ones prepared at 600°C. Namely, the SWCNT bundles in the high-temperature treated solids have irregular outer surface morphology with significant asperities, compared with the smooth outer surface in the

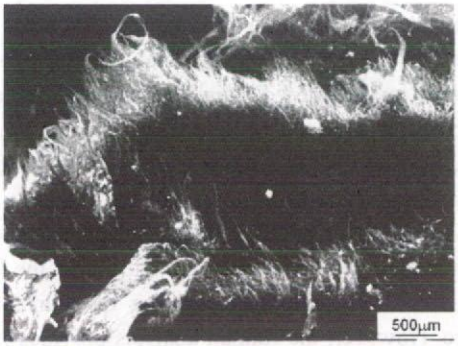

Fig. 13 SEM image of fracture surface of the SWCNT solid. (Processing condition: 1200°C, 120 MPa)

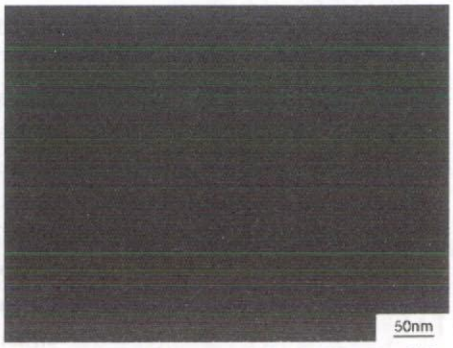

Fig. 14 TEM image of the SWCNT solid. (Processing condition: 600°C, 120 MPa)

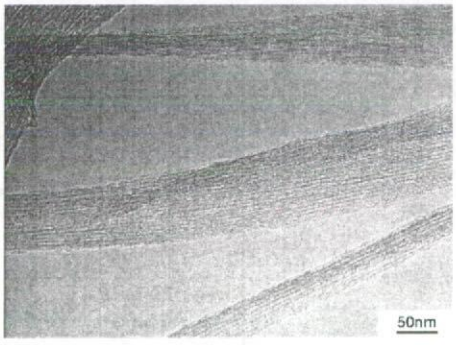

Fig. 15 TEM image of fracture surface of the SWCNT solid. (Processing condition: 600°C, 120 MPa)

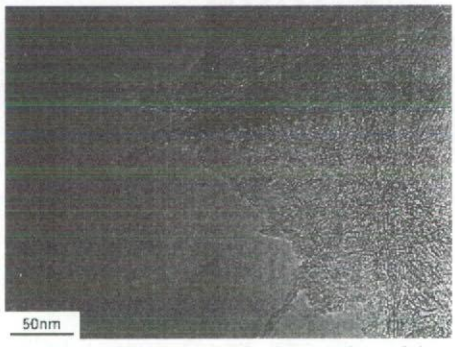

Fig. 16 TEM image of fracture surface of the SWCNT solid. (Processing condition: 1400°C, 120 MPa)

low-temperature treated solids. It is noted that SWCNT bundles are embedded in the amorphous-like structure, which is transformed from SWCNTs. The tighter links between the SWCNTs and amorphous-like structure may cause the improved mechanical properties that occur when the materials are prepared at higher sintering temperatures.

4. Summary

In this study, the SPS method was employed to solidify SWCNTs only, and the effects of processing conditions on the mechanical properties of the SWCNT solids were examined using the SP testing method. The sintering temperature used was in the range of 600~1400°C, and the sintering pressure used was 40MPa and 120 MPa. The obtained results can be summarized as follows:

(1) SWCNTs were successfully solidified without any additives by SPS.

(2) Purification of raw soot was critically important in order to improve the mechanical properties of the SWCNT solid, which exhibited a significant nonlinear deformation response in contrast with brittle fracture of the raw soot solid. The work of fracture of the SWCNT solids was 12.4 times larger than that of the raw soot solids.

(3) The Young's modulus and work of fracture of the SWCNT solids increased with the increasing sintering temperature and pressure, probably reflecting the improvement of interfacial strength between SWCNTs and amorphous-like structure transformed from SWCNTs caused by the spark plasma generated in the SPS process.

(4) The failure in the SWCNT solids occurred via intra-bundle sliding between SWCNTs, within and between the bundles.

Acknowledgments

This work was supported by the 21st Century COE Program Grant of the International COE of Flow Dynamics, and the Japan Ministry of Health, Labor and Welfare under Grants-in-Aid for Research on Advanced Medical Technology, which was supported by Ministry of Education, Culture, Sports, Science and Technology. We thank Mr. K. Motomiya of Graduate School of Engineering, Tohoku University for his technical assistance in TEM analysis.

References

(1) Iijima, S. and Ichihashi, T., Single-shell carbon nanotubes of 1-nm diameter, *Nature*, Vol. 363 (1993), pp. 603-605.

(2) Hamada, N. et al., New one-dimensional conductors: Graphitic microtubules, *Physical Review Letters*, Vol. 68, No. 8 (1992), pp. 1579-1581.

(3) Li, F. et al., Tensile strength of single-walled carbon nanotubes directly measured from their macroscopic ropes, *Applied Physics Letters*, Vol. 77, No. 20 (2000), pp. 3161-3163.

(4) Yu, M.F. et al., Tensile loading of ropes of single wall carbon nanotubes and their mechanical properties, *Physical Review Letters*, Vol. 84, No. 24 (2000), pp. 5552-5555.

(5) Yakobson, B.I. et al., Nanomechanics of carbon tubes: Instabilities beyond linear response, *Physical Review Letters*, Vol. 76, No. 14 (1996), pp. 2511-2514.

(6) Zhan, G.D. et al., Single-wall carbon nanotubes as attractive toughening agents in alumina-based nanocomposites, *Nature Materials*, Vol. 2, No. 1 (2003), pp. 38-42.

(7) Ren, Y. et al., Tension-tension fatigue behavior of unidirectional single-walled carbon nanotube reinforced epoxy composite, *Carbon*, Vol. 41, No. 11 (2003), pp. 2177-2179.

(8) Omori, M., Sintering, consolidation, reaction and crystal growth by the spark plasma system (SPS), *Materials Science and Engineering A-Structural Materials Properties Microstructure and Processing*, Vol. 287, No. 2 (2000), pp. 183-188.

(9) Okuda, S. et al., Small punch testing method for the development of functionally gradient materials, *Transaction of the Japan Society of Mechanical Engineers A*, Vol. 57 (1991), pp. 940-945.

(10) Seraphin, S. and Zhou, D., Single-walled carbon nanotubes produced at high-yield by mixed catalysts, *Applied Physics Letters*, Vol. 64, No. 16 (1994), pp. 2087-2089.

(11) Kasuya, A. et al., Evidence for size-dependent discrete dispersions in single-wall nanotubes, *Physical Review Letters*, Vol. 78, No. 23 (1997), pp. 4434-4437.

(12) Yamamoto, G. et al., Effect of impurities on mechanical properties of SWNT solids prepared by spark plasma sintering, *Proceeding of the 15th Symposium on Functionally Graded materials*, (2003-11), pp. 157-162.

(13) Saito, Y. and Bandow, S., *Introduction to Carbon Nanotube*, (1998), pp. 194-198, CORONA PUBLISHING.

(14) Chesnokov, S.A. et al., Mechanical energy storage in carbon nanotube springs, *Physical Review Letters*, Vol. 82, No. 2 (1999), pp. 343-346.

IOP PUBLISHING NANOTECHNOLOGY

Nanotechnology **18** (2007) 145614 (5pp) doi:10.1088/0957-4484/18/14/145614

Polycarbosilane-derived SiC/single-walled carbon nanotube nanocomposites

Go Yamamoto[1,4], Kenji Yokomizo[1], Mamoru Omori[1], Yoshinori Sato[2], Balachandran Jeyadevan[2], Kenichi Motomiya[2], Toshiyuki Hashida[1], Toru Takahashi[1], Akira Okubo[3] and Kazuyuki Tohji[2]

[1] Fracture and Reliability Research Institute, Tohoku University, 6-6-11-707, Aza-Aoba, Aramaki, Aobaku, Sendai 980-8579, Japan

[2] Graduate School of Environmental Studies, Tohoku University, 6-6-11-1305, Aza-Aoba, Aramaki, Aobaku, Sendai 980-8579, Japan

[3] Institute of Materials Research, Tohoku University, 2-2-1 Kataura, Aobaku, Sendai 980-8577, Japan

E-mail: gyamamoto@rift.mech.tohoku.ac.jp

Received 11 October 2006, in final form 15 January 2007
Published 8 March 2007
Online at stacks.iop.org/Nano/18/145614

Abstract

One of the key issues for the development of high toughness carbon nanotube (CNT) reinforced composites is the control of the interfacial bond between the CNT and the matrix. Here, we introduce a novel technique to facilitate the homogeneous coating of single-walled carbon nanotube (SWCNT) bundles with polycarbosilane (PCS)-derived SiC nanoparticles. The PCS dissolved in n-hexane was used as a precursor for SiC nanoparticles. The results obtained from XRD, TEM and EDXS analyses confirmed the formation of β-SiC nanoparticles of about 20 nm in diameter, which possessed a relatively homogeneous distribution on the SWCNT bundles. It was shown that the number of SiC nanoparticles per unit of SWCNT surface area could be adjusted by changing the weight ratio of PCS and SWCNTs. This approach may provide a useful route for the preparation of SiC/SWCNT nanocomposites that have a tunable interface property with the matrix and potentially with an enhanced anchor effect, which may have potential applications as a reinforcing element in CNT/ceramic composites.

1. Introduction

The unique mechanical, electrical and thermal properties of both single- and multi-walled carbon nanotubes, have attracted extensive research attention in recent years [1, 2]. Numerous investigators have reported remarkable physical and mechanical properties for this new form of carbon [3–8]. The salient feature of the carbon nanotubes (CNTs) such as the exceptional mechanical properties combined with their low-density, offers scope for the development of CNT-reinforced composite materials [9–11]. Many attempts have been made to develop advanced composite materials with CNTs as reinforcing additives in various matrices to overcome the performance limits of conventional materials.

[4] Author to whom any correspondence should be addressed.

Engineering ceramics have high stiffness, excellent thermostability and relatively low density, but their brittleness impedes their use as structural materials. Incorporating CNTs into a ceramic matrix might be expected to produce tough as well as highly stiff and thermostable ceramic composites. The matrices used for CNT-reinforced ceramic composites in the previous study were primarily Al_2O_3 and SiC [12–15]. Ma *et al* [12] synthesized a SiC/multi-walled carbon nanotube (MWCNT) composite via hot-pressing a mixture composed of SiC nanoparticles with 10 wt% MWCNTs. The authors reported a 10% improvement in the toughness and strength compared to the MWCNTs-free monolithic SiC synthesized under similar processing conditions. Wang *et al* [15] used a spark plasma sintering technique to prepare Al_2O_3 composite containing 10 vol% single-walled carbon nanotubes (SWCNTs). The authors performed single edge notched

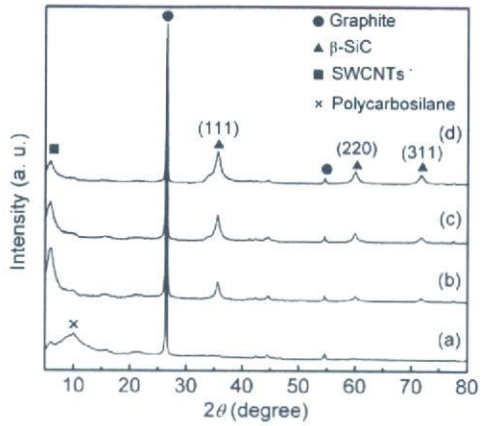

Figure 1. XRD patterns of the cured PCS–SWCNTs mixture (a) and heat-treated products with different PCS to SWCNTs weight ratios of (b) 3/7, (c) 1 and (d) 7/3.

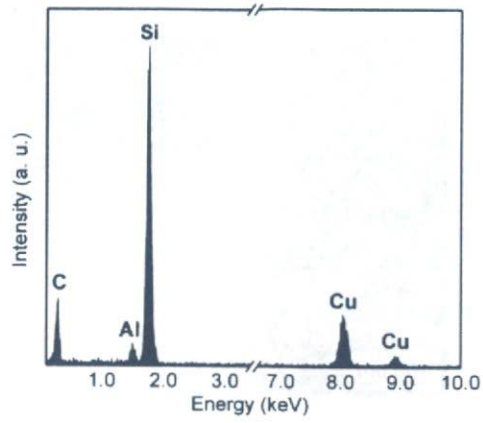

Figure 2. EDXS data taken from the nanoparticle attached to the SWCNT surface. EDXS was also done for other spots on the nanoparticle and similar signals were obtained.

beam (SENB) tests on the Al_2O_3/SWCNT and Al_2O_3-based composite containing graphite particles. The fracture toughness of the Al_2O_3/SWCNT composite measured by the SENB method was reported to be similar to that of the Al_2O_3/graphite composite, whereas the addition of SWCNTs was more effective than that of graphite in the improvement of contact-damage resistance of the composites. Although there are a small number of papers which report exceptionally large increases in the mechanical properties such as toughness, the improvement by CNT addition has been limited so far in previous studies. The primary reason for the less satisfactory improvement in toughness and strength may be due to inhomogeneous dispersion of CNTs in the matrix and the poor wettability of the CNT surface with the ceramic matrix. Therefore, we expect that the surface modification of relatively inert CNTs is vital prior to their use in ceramic composites.

It has been reported that the pyrolysis of polycarbosilane (PCS) in inert atmosphere at temperatures up to 1500 °C results in the formation of SiC via metastable phases such as the Si–O–C phase [16, 17]. In this study, we introduce a novel technique to facilitate the homogeneous coating of SWCNT bundles with the SiC nanoparticles using PCS as the source of SiC, with the objective of improving the wettability of the SWCNT surface with the ceramic matrix. Unlike conventional coating techniques [18–20], the synthesis of nanocomposites was attempted by facilitating the formation of the SiC nanoparticles from a PCS dissolved in n-hexane in which the SWCNTs are dispersed. In this paper, the synthesis procedure and characterization of the PCS-derived SiC/SWCNT nanocomposites are presented.

2. Experimental procedure

The preparation of the highly pure SWCNTs was carried out using the technique described elsewhere [21, 22]. The purified SWCNTs used in this study were prepared by subjecting the soot synthesized by an arc discharge method to heat treatment under an oxidizing atmosphere and chemical treatment in hydrochloric acid. The estimated SWCNT diameter and bundle length of purified SWCNTs from Raman scattering measurement and scanning electron microscopy ranged between 1.33–1.52 nm and 1.5–22.0 μm, respectively.

In this study, three kinds of PCS-derived SiC/SWCNT nanocomposites with PCS/SWCNTs weight ratios of 3/7, 1 and 7/3 were synthesized by pyrolysis of PCS in the PCS–SWCNTs mixture. The synthesis procedure for the nanocomposite preparation is as follows. First, solid-state PCS (Nippon Carbon, Japan) was put in a beaker containing 50 ml of n-hexane (Kanto Chemical, Japan), and ultrasonically dissolved using a desktop type ultrasonic cleaner (US-3 SND, Japan). Then, the purified SWCNTs were introduced to the solution containing the PCS and ultrasonically dispersed for 15 min. The resultant suspension was then dried naturally in a draft chamber at 25 °C in order to remove n-hexane. Then, the PCS–SWCNTs mixture was put into a half-quartz tube and was cured at 230 °C for 15 min under an oxidizing atmosphere, in order to prevent agglomeration of PCS during subsequent high temperature treatments. Finally, the product obtained in the previous step was heat-treated at 1400 °C in vacuum for 30 min.

The structural analysis of the products was carried out using a powder x-ray diffractometer (M21 Mac Science, Japan) with Cu Kα x-ray source (λ = 1.540 56 Å). The morphology and elemental analysis of the products were carried out using a transmission electron microscope (TEM; HF-2000 Hitachi, Japan), and an energy-dispersive x-ray spectroscope (EDXS; Vantage EDX systems, NORAN instruments, USA). For TEM observation, the sample was ultrasonically dispersed in ethanol and the suspension was dropped onto a carbon-coated copper grid.

3. Results and discussion

Figure 1 shows the XRD patterns of the cured PCS–SWCNTs mixture (a) and heat-treated products with different PCS/SWCNTs weight ratios (b)–(d). The weight ratio of PCS/SWCNTs in the spectra (b), (c) and (d) is 3/7, 1 and 7/3, respectively. The XRD patterns exhibited the peaks

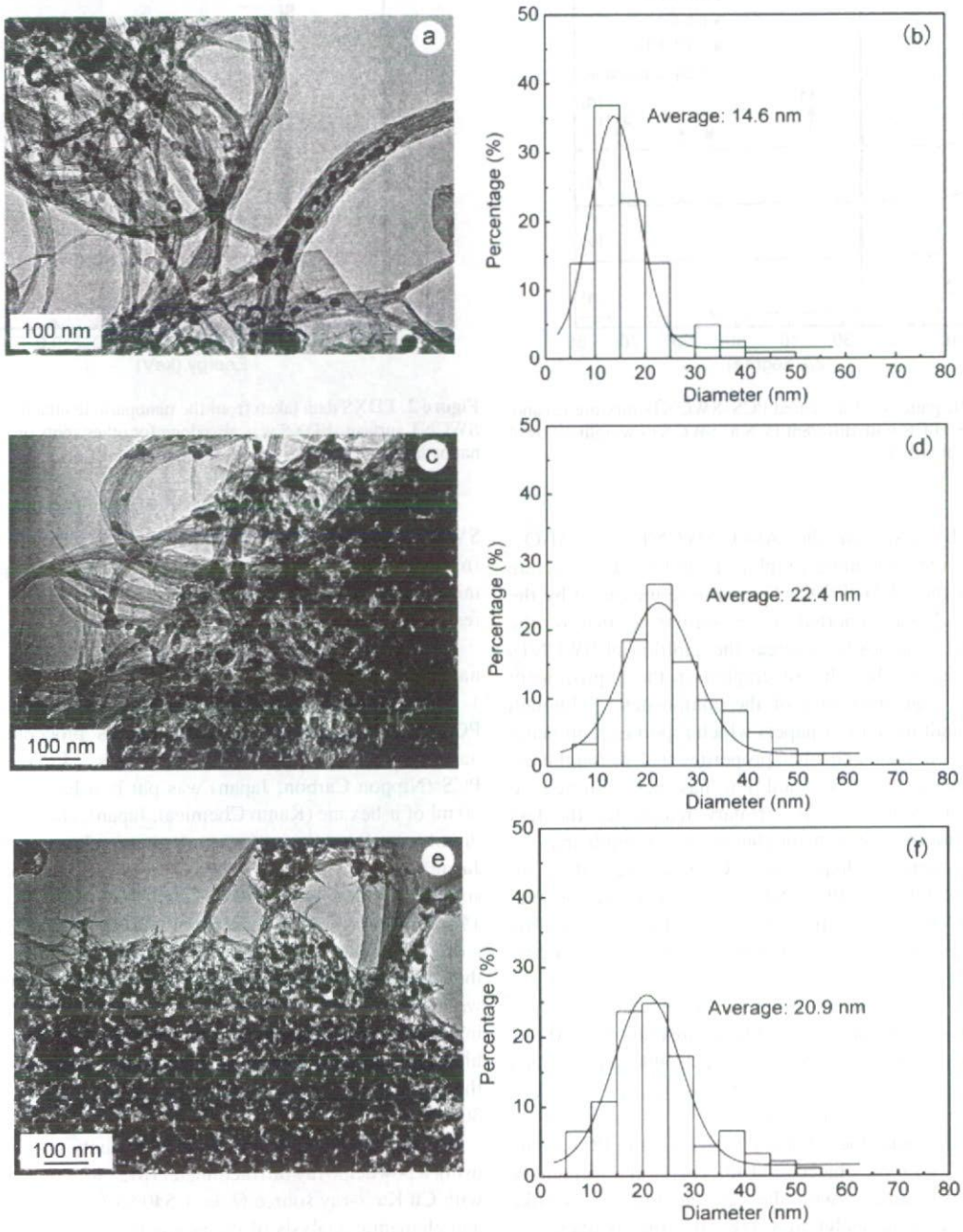

Figure 3. Typical low-magnification TEM images of the heat-treated products synthesized with different PCS/SWCNTs weight ratios of (a) 3/7, (c) 1 and (e) 7/3. (b), (d), (f) Corresponding size distribution of the SiC nanoparticles in samples (a), (c), (e), respectively. The solid lines in (a), (c), (e) represent the Gaussian fitting curves.

corresponding to (002) and (004) planes of crystalline graphite in all of the samples. These may be attributed to the presence of carbonaceous materials different from SWCNTs, as stated in our previous report [21]. The diffraction peak corresponding to PCS at $2\theta = 10.0^{\circ}$ [16] was observed in the sample (a). However, the diffraction peak disappeared completely in the heat-treated products (b)–(d), suggesting the decomposition of PCS to form β-SiC. The peaks corresponding to (111), (220) and (311) planes of β-SiC are observed for all of the heat-treated products. These data clearly indicate that β-SiC was successfully synthesized by the pyrolysis of PCS at 1400 °C. The crystallite size (L) in the direction parallel to the (111) plane of the β-SiC were obtained from the Scherrer equation [23] using the equation $L = 0.9\lambda/\beta\cos\theta$, where λ is the x-ray wavelength, β is the full-width at half-maximum (FWHM) intensity of the (111) plane, and θ is the Bragg angle. For the heat-treated products with PCS/SWCNTs weight ratios of 3/7, 1 and 7/3, L was 8.9, 9.1 and 7.1 nm,

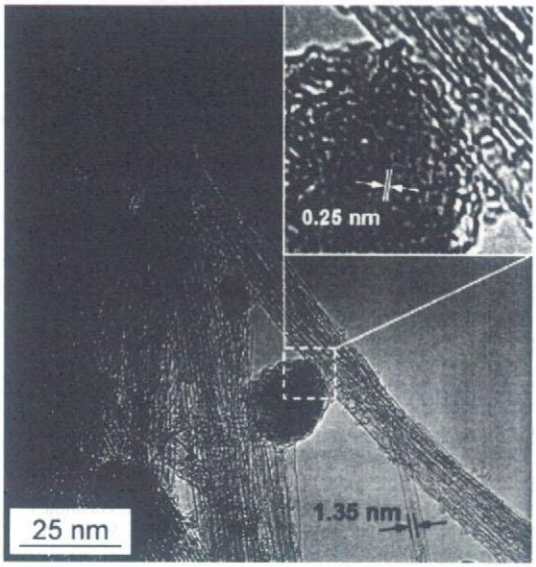

Figure 4. Typical high-magnification TEM image of the nanocomposite, showing the PCS-derived SiC nanoparticles on the SWCNT bundle. Enlarged TEM image, taken from the dashed line square area.

respectively. The results agree well with the L of the SiC materials synthesized by pyrolysing PCS [24]. A detailed morphological investigation of the heat-treated products was carried out using TEM.

The TEM observations confirmed the formation of spherical-shaped nanoparticles with diameters of about 10–20 nm attached to the SWCNT bundles, as shown in figures 3(a), (c) and (e). The chemical composition of the nanoparticles was further confirmed by TEM–EDXS. The spectrum obtained by narrowing down the beam and focusing the beam directly onto the nanoparticle attached to the SWCNT bundle recorded C, Al, Si and Cu, as shown in figure 2. Here, the Cu and Al peaks originated from the copper grid and the aluminium support on which the copper grid rests. On the other hand, the Si peak was hardly observed when there were no nanoparticles in the observation spot. Thus, the EDXS analysis clearly indicates that the nanoparticles are composed of C and Si. Quantitative analysis revealed that the nanoparticles are composed of Si/C with an atomic ratio of about 2.2/7.8, and not equal to the stoichiometric proportion of SiC, which was probably due to the presence of the amorphous carbon surrounding the nanoparticles (shown in figure 4) and the neighbouring SWCNTs. In addition, it is well accepted that the free carbon exists in the PCS-derived SiC materials [24].

Figures 3(a)–(f) show the typical low-magnification TEM images of a series of the PCS-derived SiC/SWCNT nanocomposites and the corresponding size distributions of the SiC nanoparticles synthesized with the different PCS to SWCNTs weight ratios. Here, the histograms of particle size distributions were obtained using TEM images. It is clear from figures 3(b), (d) and (f) that the size of the SiC nanoparticles is on the nanoscale and the average size is in the range of 14.6–22.4 nm for the PCS contents used in this study. We can see that the SiC nanoparticle density, namely the number of SiC nanoparticles per unit of SWCNT surface area increases with the increase in the PCS to SWCNT weight ratio. Hereafter, the number of SiC nanoparticles per unit of SWCNT surface area is referred to as the SiC nanoparticle density. In addition to the SiC nanoparticle density, the average size of the SiC nanoparticles appears to vary with respect to the PCS content. When the PCS content increases from 3/7 to 1, the average size of the SiC nanoparticles increases from 14.6 to 22.4 nm. On the other hand, when the PCS content further increases to 7/3, no substantial change in the nanoparticle size is observed. The above observation suggests that the average size of the SiC nanoparticles may increase initially with the increasing PCS content and then level off when the PCS/SWCNTs weight ratio exceeds about 1, even though further detailed tests need to be carried out in order to clarify the effect of the PCS content on the SiC nanoparticle size. The experimental results demonstrate that the present method, which uses the organic precursor (i.e. PCS), may provide an effective route for coating SWCNTs with SiC nanoparticles, and that it may be possible to adjust and control the SiC nanoparticle density and average size by varying the PCS/SWCNTs weight ratio. It is well known that the size of nanoparticles deposited on CNTs synthesized using vapour methods depends strongly on the processing time [25, 26]. Kuang *et al* [25] demonstrated that prolonging the deposition time could control the sizes of the SnO_2 nanoparticles synthesized using chemical vapour deposition and deposited on the MWCNT surface. Thus, we expect that varying the heat treatment time may also provide a means for controlling the size of the SiC nanoparticle in the PCS-derived SiC/SWCNT nanocomposites.

Figure 4 shows a high-magnification TEM image of the SWCNT bundles with the SiC nanoparticles. The diameter of the SWCNTs has been determined to be about 1.35 nm, suggesting that no change in the SWCNT diameter occurred during the pyrolysis of PCS at 1400 °C in vacuum. The detailed structural information of the SiC nanoparticles was retrieved from the enlarged TEM image. The crystalline fringe of the SiC nanoparticles with a lattice spacing of about 0.25 nm is in good agreement with the lattice fringe (111) of β-SiC (JCPDS card No. 29-1129). At the same time, the interface between the SiC nanoparticle and SWCNTs appears to be smooth, suggesting the formation of direct bonding of the nanoparticle to the SWCNT surface. The above-mentioned bonding may be due to the good wettability of the PCS-derived SiC nanoparticles and SWCNT surface. Indeed, when the PCS-derived SiC/SWCNTs nanocomposites were subjected to ultrasonic agitation in ethanol, no detachment of the SiC nanoparticles was detected using TEM observation. Thus, it is expected that the present organic precursor technique may be useful to produce a relatively strong interfacial bond between SiC nanoparticles and SWCNTs.

4. Conclusion

In this study, we have demonstrated the preparation of SiC/SWCNT nanocomposites by pyrolysis of polycarbosilane at 1400 °C in vacuum. The experimental results revealed the formation of β-SiC nanoparticles 14.6–22.4 nm in average size, which possess a homogeneous distribution on the SWCNT bundles. The SiC nanoparticle density and average size of the SiC nanoparticles were shown to depend on the

weight ratio of PCS and SWCNTs. This approach may provide a useful route for the preparation of SiC/SWCNT nanocomposites that have a tunable interface property with the matrix and potentially with an enhanced anchor effect, which may have potential applications as a reinforcing element in CNT/ceramic composites. Furthermore, by choosing different kinds of organic precursors, many other nanoparticles such as Si–C–N [27, 28] may be selectively deposited onto SWCNTs.

Acknowledgments

This work was supported by the 21st Century Center of Excellence (COE) Program Grant of the International COE of Flow Dynamics, Ministry of Education, Culture, Sports, Science and Technology.

References

[1] Baughman R H, Zakhidov A A and de Heer W A 2002 *Science* **297** 787
[2] Terrones M 2003 *Annu. Rev. Mater. Res.* **33** 419
[3] Kong J, Franklin N R, Zhou C, Chaplin M G, Peng S, Cho K and Dai H 2000 *Science* **287** 622
[4] Bachtold A, Hadley P, Nakanishi T and Dekker C 2001 *Science* **294** 1317
[5] Falvo M R, Taylor R M, Helser A, Chi V, Brooks F P, Washburn S and Superfine R 1999 *Nature* **397** 236
[6] Salvetat J P, Briggs G A D, Bonard J-M, Bacsa R R, Kulik A J, Stockli T, Burnham N A and Forro L 1999 *Phys. Rev. Lett.* **82** 944
[7] Yu M-F, Files B S, Arepalli S and Ruoff R S 2000 *Phys. Rev. Lett.* **84** 5552
[8] Yu M-F, Lourie O, Dyer M J, Moloni K, Kelly T F and Ruoff R S 2000 *Science* **287** 637
[9] Thostenson E T, Ren Z and Chou T-W 2001 *Compos. Sci. Technol.* **61** 1899
[10] Curtin W A and Sheldon B W 2004 *Mater. Today* **7** 44
[11] Harris P J F 2004 *Int. Mater. Rev.* **49** 31
[12] Ma R Z, Wu J, Wei B Q, Liang J and Wu D H 1998 *J. Mater. Sci.* **33** 5243
[13] Flahaut E, Peigney A, Laurent Ch, Marliere Ch, Chastel F and Rousset A 2000 *Acta Mater.* **48** 3803
[14] Peigney A, Laurent Ch, Flahaut E and Rousset A 2000 *Ceram. Int.* **26** 677
[15] Wang X, Radture N P and Tanaka H 2004 *Nat. Mater.* **3** 539
[16] Yajima S, Hayashi J, Omori M and Okamura K 1976 *Nature* **261** 683
[17] Hasegawa Y, Iimura M and Yajima S 1980 *J. Mater. Sci.* **15** 720
[18] Morisada Y, Maeda M, Shibayanagi T and Miyamoto Y 2004 *J. Am. Ceram. Soc.* **87** 804
[19] Jitianu A, Cacciaguerra T, Benoit R, Delpeux S, Beguin F and Bonnamy S 2004 *Carbon* **42** 1147
[20] Ravindran S and Ozkan C S 2005 *Nanotechnology* **16** 1130
[21] Yamamoto G, Sato Y, Takahashi T, Omori M, Hashida T, Okubo A, Watanabe S and Tohji K 2005 *J. Mater. Res.* **20** 2609
[22] Yamamoto G, Sato Y, Takahashi T, Omori M, Okubo A, Tohji K and Hashida T 2006 *Scr. Mater.* **54** 299
[23] Lipson H and Steeple H 1970 *Interpretation of X-ray Powder Diffraction Patterns* (New York: St Martin's Press)
[24] Yajima S, Okamura K, Hayashi J and Omori M 1976 *J. Am. Ceram. Soc.* **59** 324
[25] Kuang Q, Li S-F, Xie Z-X, Lin S-C, Zhang X-H, Xie S-Y, Huang R-B and Zheng L-S 2006 *Carbon* **44** 1166
[26] Zhu Y, Elim H I, Foo Y-L, Yu T, Lin Y, Ji W, Lee J-Y, Shen Z, Wee A T-S, Thong J T-L and Sow C-H 2006 *Adv. Mater.* **18** 587
[27] Seyferth D, Wiseman G H and Prudhomme C 1983 *J. Am. Ceram. Soc.* **66** C13
[28] Penn B G, Ledbetter F E, Clemons J M and Daniels J G 1982 *J. Appl. Polym. Sci.* **27** 3751